EES Catalysis

PAPER

View Article Online
View Journal | View Issue

Cite this: *EES Catal.*, 2025, 3, 1302

Visualizing degradation mechanisms in a gas-fed CO_2 reduction cell *via operando* X-ray tomography

Sol A Lee,[a] Myeong Je Jang,[a] Zhiyuan Qi,[a] Kaiwen Wang,[a] Ian Sullivan,[a] Laura Paradis-Fortin,[b] Dilworth Y. Parkinson,[c] Walter S. Drisdell, *[b] Harry A. Atwater *[a] and Chengxiang Xiang *[a]

We utilize *operando* X-ray computed tomography, coupled with real-time electrochemical analysis, to reveal the underlying failure mechanisms of membrane electrode assemblies (MEAs) for electrochemical CO_2 reduction (eCO_2R). Through *operando* imaging, we can obtain unprecedented insights into the dynamic behavior of the MEA under different operating conditions, revealing critical changes in interface interactions, phase distribution, and structural integrity over time. Our findings identify phenomena giving rise to the transition from CO_2R to the hydrogen evolution reaction (HER), as evidenced by shifts in cathode potential and CO_2R selectivity. The formation of inhomogeneous precipitates at the gas diffusion electrode disrupts the CO_2 supply and reduces the active sites for eCO_2R, resulting in a shift toward H_2 production during low current density operation. Additionally, under high current density conditions, rapid water crossover up to the microporous layer/gas diffusion layer promotes the transition from CO_2R to HER, further shifting cell potential toward anodic direction. Oscillating voltage conditions reveal the dissolution and regrowth of precipitates, providing direct visualization of the competing selectivity of CO_2R and HER. This work offers new insight into the degradation mechanisms of MEAs, with implications for the design of more durable CO_2R systems.

Received 29th July 2025,
Accepted 1st August 2025

DOI: 10.1039/d5ey00232j

rsc.li/eescatalysis

Broader context

Converting waste CO_2 into value-added fuels and chemicals using renewable electricity is a net-zero carbon emission technology that addresses climate change caused by greenhouse gas emissions. Zero-gap membrane electrode assemblies (MEA) utilizing a gas diffusion electrode are promising electrochemical reactor designs for high-rate CO_2 reduction. However, key challenges for MEA operation in electrochemical CO_2 reduction (eCO_2R) include salt precipitation and flooding at the gas diffusion electrode (GDE), which limit stability. Despite their importance, the failure mechanisms behind these issues are not yet fully understood. We report direct visualization of the dynamic behavior and structural changes of the MEA under various operating conditions, using *operando* X-ray computed tomography, coupled with real-time electrochemical analysis. This powerful *operando* analytical approach provides insights into MEA degradation mechanisms, providing guidance for future design strategies to achieve stable CO_2R MEA operation.

Introduction

Carbon dioxide reduction powered by renewable electricity (eCO_2R) is a promising technology for generating value-added fuels and chemicals, contributing to carbon neutralization.[1] Electrochemical reactors typically use aqueous electrolytes; however, the low solubility of CO_2 in aqueous solutions leads to mass-transport and diffusion-limited reactions, restricting current density to $\sim$35 mA cm^{-2}.[2–4] In this context, gas-fed, zero-gap membrane electrode assembly (MEA) using gas diffusion electrode (GDE) has emerged as the most promising reactor design for industrial-scale applications.[5] High-rate CO_2R using MEA has been achieved with copper (Cu)-based catalysts, the only material capable of converting CO_2 to C_{2+} products.[6,7] However, the MEA remains limited in terms of long-term stability under the required commercial operational current densities.

The main degradation phenomena are salt precipitation, which blocks the CO_2 diffusion channels, and flooding that

[a] *Department of Applied Physics and Materials Science, California Institute of Technology, Pasadena, 91125, CA, USA. E-mail: haa@caltech.edu, cxx@caltech.edu*
[b] *Chemical Sciences Division, Lawrence Berkeley National Laboratory, Berkeley, CA 94720, USA. E-mail: wsdrisdell@lbl.gov*
[c] *Lawrence Berkeley National Laboratory, Berkeley, CA 94720, USA*

hinders the CO_2 supply and transit CO_2R to the hydrogen evolution reaction (HER). eCO_2R at high current densities generates hydroxide ions (OH^-) at the cathode, raising the local pH near the cathode surface and driving CO_2 to react with OH^- to form bicarbonates (HCO_3^-), which further convert into carbonates (CO_3^{2-}).[3,8] Concurrently, potassium ions (K^+) from the anode diffuse to the cathode side, where they react with bicarbonates and carbonates to form salts, hindering CO_2 supply and lowering eCO_2R. In addition, the application of high reduction potential can drag water from the anolyte to the cathode, altering its hydrophobicity, wetting the GDE, and causing flooding.[9,10] There have been efforts to mitigate precipitation and flooding through increasing water content and pulse operation (operation/regeneration), operation in acidic electrolytes, and operation at elevated temperatures, leading to enhanced stability.[11–17] However, it still requires a deeper understanding of the underlying progress of degradation mechanisms during operation.

While *ex situ* analysis methods have provided valuable insights into MEA degradation, they primarily capture static snapshots of post-mortem samples.[18] To address this gap, monitoring the primary degradation phenomena of MEA has been advanced with *in situ*/*operando* techniques.[19–23] For example, Moss *et al.* used *operando* X-ray diffraction (XRD) to identify the cause of cell performance degradation, demonstrating that salt formation exacerbates electrolyte flooding, leading to selectivity changes under eCO_2R conditions.[24] Disch *et al.* employed high-resolution neutron imaging to study salt precipitation and water transport in a zero-gap CO_2R cell.[25] However, a missing piece remains in the systematic investigation of the intermediate stage for MEA degradation caused by the propagation of precipitation, flooding, and mechanical deformation within the GDE under operating conditions. Studies have monitored the backside of the GDE or in the gas flow channels, and although some of the measurements can provide detailed chemical information, they cannot reveal the morphological changes within the GDE. X-ray tomography offers a promising approach for studying electrochemical cell dynamics by enabling non-destructive observation of solid/liquid/gas interfaces, 3D voids, defects, and phase distribution.[26–28] These capabilities motivate the investigation of the predominant failure mechanisms of eCO_2R cells by tracking structural phase changes over time under various conditions.

In this work, we employ *operando* synchrotron X-ray tomographic imaging combined with real-time electrochemical measurement to link the microscopic morphological changes in Cu GDE with their degradation behavior. We correlate variations in electrochemical performance (*e.g.*, voltage and selectivity) with observed precipitation and flooding phenomena at the MEA, revealing the predominant failure mechanisms under different operating conditions. Our findings provide direct observations of the transition from CO_2R to HER, driven by shifts in cathode potential and CO_2R selectivity. We first visualize inhomogeneous precipitates at the Cu/membrane interface, which block the CO_2 supply and reduce the number of active sites, leading to increased H_2 production. Oscillating voltage conditions enable us to visualize the dissolution and regrowth of precipitates, highlighting the competing dynamics between CO_2R and HER. Lastly, at high current densities, we track predominant water crossover and subsequent salt precipitation at the microporous layer (MPL)/gas diffusion layer (GDL) interface, which accelerates the transition from CO_2R to HER. By identifying key failure pathways, our study provides insights that can guide the design of more durable MEAs, ultimately improving the viability of eCO_2R for large-scale carbon utilization.

Results and discussion

Design of CO_2 reduction cell for *operando* X-ray tomography measurement

The continuous projection of MEA was probed by a synchrotron X-ray beam to investigate the failure mechanism of MEA over time. Fig. S1 (SI) shows the synchrotron instrumentation setup at the Advanced Light Source 8.3.2. X-ray computed tomography beamline, which includes X-ray photon source, rotating beamline stage, and detector. X-ray tomography provided a high spatial resolution of 0.65 μm. The design of the eCO_2R reactor for X-ray micro-computed tomography (micro-CT) imaging is depicted in Fig. 1a. The cell diameter was 3.6 cm, chosen to minimize the loss of X-ray beam intensity due to penetration. The custom-designed MEA was assembled using plastic bolts. The MEA was placed on top of the rotating stage, and the leakless Ag/AgCl reference electrode was positioned at the bottom of the anode chamber to prevent disruption during the rotating projection. Fig. 1b shows a 3D view of pristine MEA before electrochemical measurements, as well as representative 2D micro-CT images of each component. The image contrast depends on the absorption coefficient of materials; metal absorbs more X-rays than polymers and carbon materials. To prevent signal interference from a metal anode, a spacer was positioned between the anion exchange membrane (AEM) and the anode. All X-ray tomography images in this study were obtained by selecting a region of interest (ROI) at the center of Cu GDE, just below the titanium rod (current collector) in the cell. Since the reconstruction process inverts the contrast of the original measurements, the Cu layer appears brighter than the carbon fibers or membrane.

The GDE used in this study featured hydrophobic MPL to prevent rapid electrolyte flooding, a common design in large-scale MEA for eCO_2R.[29] The 300 nm-thick Cu catalyst layer was observed as a thin white layer that overlaps with the AEM and MPL in the 2D slice. The components of the MEA are shown in Fig. S2a (SI). Scanning electron microscope (SEM) images (see Fig. 1c) reveal the surface morphology of carbon paper, which features randomly distributed trenches, and the particle-shaped Cu catalysts formed on carbon paper (Fig. S2b, SI). Before performing the electrochemical measurement, cross-sectional micro-CT images of the pristine MEA without flowing electrolytes were taken (marked by the blue dotted line in Fig. S2c, SI) to confirm the initial microstructural features of

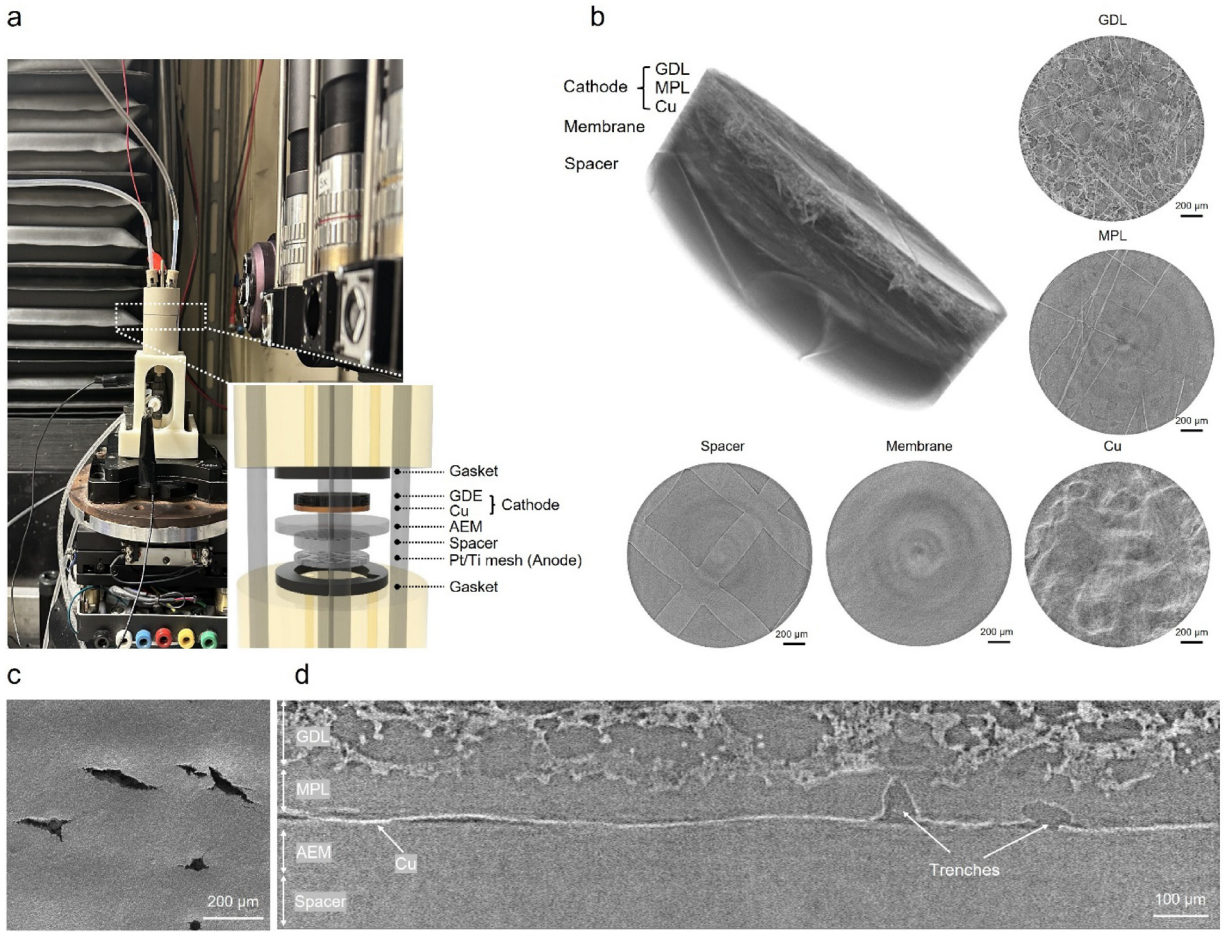

Fig. 1 *Operando* X-ray tomography measurement with zero-gap MEA. (a) Photograph of eCO_2R cell in the X-ray tomography measurement setup. The schematic shows the components of the eCO_2R cell. (b) 3D stack and selected 2D slices of MEA before eCO_2R, highlighting each component. (c) SEM image of the MPL side of the carbon paper. (d) Cross-sectional micro-CT image of MEA before eCO_2R measurement.

the MEA. Distinguishable components were observed in the cross-sectional micro-CT images: the GDL exhibited a porous microstructure, the MPL showed a relatively uniform intensity, the Cu layer appeared as a bright, thin layer, and both the AEM and spacer had a uniform contrast distribution. As shown in Fig. 1d, the trenches in the MPL appear as darker intensity holes, which match the top-view SEM image (Fig. 1c).

Visualization of failure mechanisms of MEA during eCO_2R

The behavior of the Cu GDE is influenced by the applied current density and electrolyte concentration, both of which affect both selectivity and stability.[30] In the MEA system, maintaining an appropriate water content is crucial for establishing an efficient triple-phase interface between CO_2 (gas), electrolyte (liquid), and catalyst (solid) for eCO_2R.[3,12,31,32] As the applied current increases, the amount of water electro-dragged to the cathode also increases. Excessive water reduces the hydrophobicity of the GDL, thereby impairing mass transport and ultimately leading to a loss in both selectivity and stability.[33] In addition, at higher current densities, precipitation on the GDE due to electrolyte infiltration blocks the CO_2 supply, promoting HER over CO_2R.[9,20,34] Therefore, the primary focus of this study is to track structural changes in the Cu GDE caused by precipitation and flooding and to elucidate the predominant degradation mechanisms.

Shift from CO_2R to HER by predominant precipitate growth

To obtain micro-CT images, a modification of the cell was required, involving the introduction of a mesh-type Nylon spacer between the anode and membrane to mitigate interference from the metallic anode signal when analyzing the membrane/Cu catalyst interface. The addition of the spacer increased the ohmic resistance and hindered mass transport kinetics, requiring more negative potential to achieve the desired current density (Fig. S3, SI). Despite the decreased current density generated from the modified MEA, the insights from *operando* micro-CT are valuable. We initially conducted eCO_2R at -50 mA cm^{-2} for 20 h under 0.1 M $KHCO_3$ to minimize water crossover. As shown in Fig. S4a (SI), the MEA primarily converted CO_2 to CO, exhibiting a slight decrease in CO selectivity and an increase in cathode potential. Given the limited time available at the synchrotron, we operated the MEA at a selected current density of -50 mA cm^{-2} in 0.1 M for $KHCO_3$ for 7 hours. Under this condition, the Cu GDE

maintained a stable potential profile and selectivity distribution, primarily for CO and H_2 (see Fig. S4b and c, SI). Comparing cross-sectional tomography images of the MEA every hour, a small amount of the precipitates was observed near the MPL/Cu interface (see Fig. S4d, SI).

We then compared the behavior of Cu GDE at higher operating current density, where Cu catalysts can promote the conversion of CO_2 to C_2 products (see Fig. S5, SI). Ethylene selectivity was observed at an operating current density of -100 mA cm^{-2}, with an approximate 10% ethylene selectivity. The total faradaic efficiency (FE) remained below 100%, which could be attributed to the exclusion of liquid products in the FE calculation. Some liquid products might have diffused to the anode side and undergone oxidation. The Cu GDE showed the oscillating voltage profile and subsequent FE fluctuations after 7 hours of operation. When the MEA was operated at high-concentration (0.5 M, 1 M) $KHCO_3$ electrolytes, the Cu GDE showed an increase in H_2 selectivity with voltage oscillation or complete H_2 evolution (see Fig. S6, SI).

We investigated the interface dynamics and morphological change of the MEA under conditions where the Cu GDE exhibits high ethylene selectivity. As shown in Fig. 2a, a shift in selectivity was observed over 1 hour of operation, with an increase in H_2 selectivity and a decrease in CO_2R activity. To track the structural change and interface dynamics, we obtained visualized interior images of the MEA at 0.2 h intervals. As shown in Fig. 2b, a white, particle-shaped structure was identified at the 2D micro-CT image showing MPL/Cu/membrane interface. Inhomogeneous precipitate formation, distribution, and growth were observed over time. The extent of precipitate growth reached the MPL during operation, as confirmed by comparing the MPL, GDL/MPL and GDL region (see Fig. S7, SI) and analyzing the cross-sectional micro-CT images (Fig. S8, SI). Notably, precipitation led to mechanical deformation of the Cu/membrane interface, a phenomenon observed for the first time in this study.

Voltage oscillation and transition between CO_2R and HER

Voltage oscillations and subsequent changes in selectivity are commonly observed when the MEA approaches a stability boundary condition, as reported in the literature.[24,35] For example, Mikami *et al.* observed oscillations in a 5 cm^2-size zero-gap cell using a real-time CMOS camera, monitoring the flow channels.[35] To gain a deeper understanding of the dynamics behind the fluctuations in eCO_2R performance, we operated the MEA at current densities of -150 mA cm^{-2} and -200 mA cm^{-2} in 0.1 M $KHCO_3$, where voltage oscillations were observed within a reasonable timescale (a few hours). At a current density of -150 mA cm^{-2}, the MEA exhibited small voltage oscillations between 1 and 3 hours of operation, accompanied by transient changes in voltage profile and CO_2R selectivity (Fig. S9a, SI). We correlated the observed oscillatory behavior of the Cu GDE with *operando* micro-CT images. The selectivity changes and potential shifts between points 3 to 6, where the voltage oscillation occurred, were analyzed through micro-CT images. The precipitates were observed to dissolve as the potential fluctuated, evidenced by the variation in precipitate contrast, and began to re-grow after point 6 (see Fig. S9b, SI). Cross-sectional micro-CT images of MEA (see Fig. S10, SI) provide further support for the extent of precipitate dissolution during the oscillatory cycle. After the dissolution of precipitates at point 4, the precipitates began to re-grow in the same locations. A few large potential drops (see Fig. S9a, SI) do not indicate voltage oscillation but may be attributed to the capture of oxygen bubbles near the reference electrodes or the confinement of oxygen bubbles in the anode chamber.

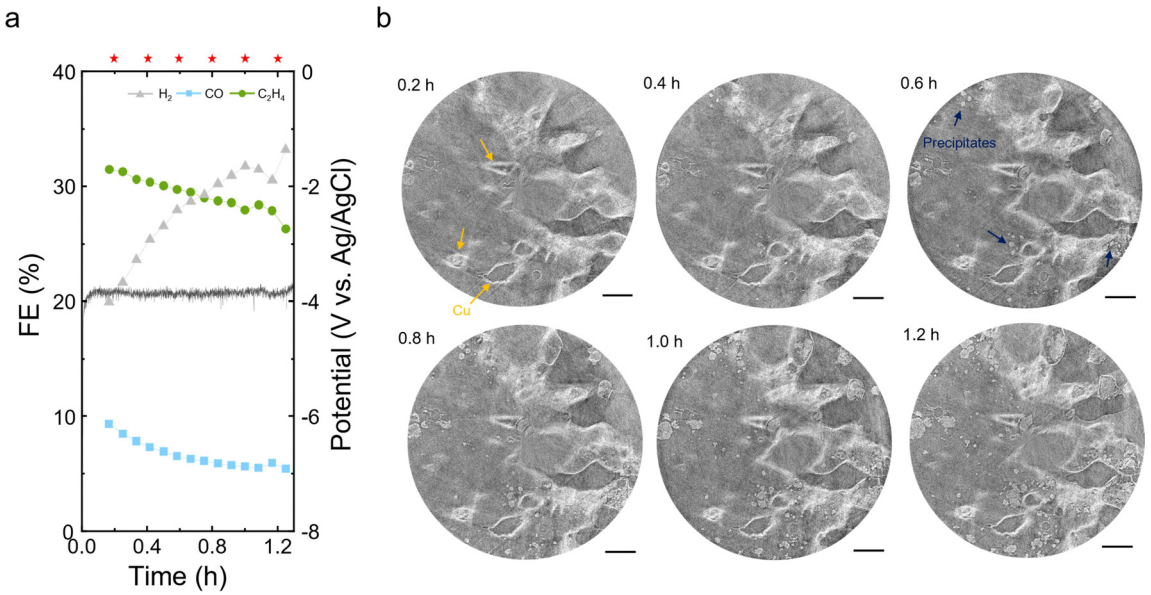

Fig. 2 Formation of precipitates during eCO_2R. (a) FE and chronopotentiometry curve of Cu GDE at a current density of -150 mA m^{-2}. (b) 2D X-ray tomography images at the Cu/membrane interface at different reaction times (indicated as red star marks). The scale bar represents 200 μm.

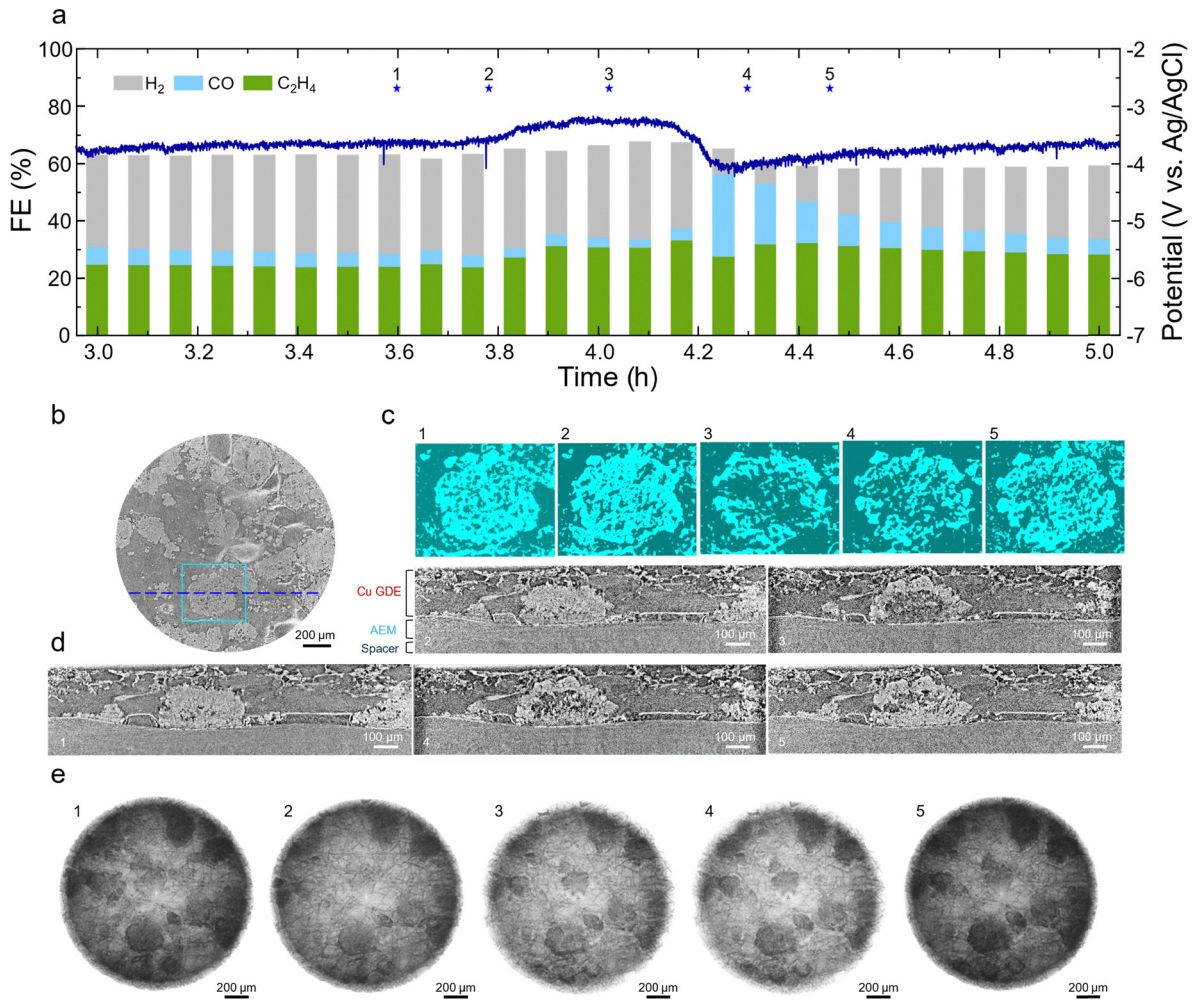

Fig. 3 Dissolution and regrowth of precipitates during eCO_2R. (a) FE and chronopotentiometry curve of Cu GDE at a current density of −150 mA m^{-2}. (b–e) X-ray tomography images of MEA, all obtained at the blue star marks with numbers. (b) 2D X-ray tomography image of MPL/Cu interface at point 1. (c) Segmented images showing precipitate dissolution and regrowth during eCO_2R (area indicated by a cyan box in b). (d) Cross-sectional tomography images. The position of the cross-sectional images is indicated by the blue dash line in b. (e) Corresponding 3D micro-CT images of Cu GDE.

We found noticeable evidence of interface dynamics and phase distribution changes during the oscillatory period. As the voltage shifted anodically, C_2H_4 selectivity slightly increased (see Fig. 3a). Prior to the voltage fluctuation (point 1), a significant number of precipitates were distributed at the MPL/Cu (Fig. 3b). To track the changes in precipitation over time, we performed segmentation on the region marked by a cyan box in Fig. 3b, using 2D slices at the same height and position of the Cu GDE. At the beginning of the transient period (point 2), the FE remained stable, while the segmentation image revealed the partial dissolution of the precipitates (Fig. 3c). When the MEA entered the anodically shifted potential region (point 3), a decrease in H_2 and CO selectivity, alongside an increase in C_2H_4 selectivity, was observed, followed by significant dissolution of the salt precipitates.

Cross-sectional micro-CT images (see Fig. 3d) illustrate the extent to which precipitates grow from the Cu/membrane interface to the GDL. The cross-sectional image was taken from the position marked by the green line in Fig. 3b. At point 2, a solution signal was detected in the gap between the Cu GDE and the membrane, accompanied by a reduced contrast of precipitates near the Cu/membrane interface, indicating partial dissolution. Further hollow structures of precipitates were observed at point 3, likely due to significant water crossover. From the observed morphological changes in the precipitates, it can be inferred that water did not reach the GDL, resulting in relatively stable H_2 selectivity. After water crossover, the Cu GDE exhibited an increase in active sites for eCO_2R due to the removal of precipitates at the MPL and membrane/Cu interface, resulting in a voltage drop and a shift from HER to CO_2R, with an increase in CO selectivity. As the reaction continued, regrowth of the precipitates gradually filled the hollow spaces. Furthermore, by comparing the images at points 1 and 5, we observed that the precipitation eventually reached the GDL. 3D micro-CT images (see Fig. 3e) further support the precipitation, dissolution, and regrowth within the GDE, with varying density and distribution of precipitates.

The MEA exhibited repeating oscillatory behavior over 7 hours of operation (see Fig. S11, SI). A comparison of cell potentials at the

beginning of the measurement (0 h) and after 6 hours revealed anodic potential shifts of 0.3–0.4 V. As shown in Fig. S11b (SI), a significant accumulation of precipitates was observed at the MPL/GDL, though some precipitates were dissolved during the oscillatory period. Notably, the 2D images confirmed the dissolution of precipitates at the MPL/GDL, implying that water had reached this region. The invasion of water into the GDL can alter the hydrophobic nature of the GDE to hydrophilic, which in turn may trigger a shift from eCO_2R to HER. The salt precipitates formed on Cu GDE were K_2CO_3 and $KHCO_3$ (see Fig. S12, SI).

The voltage oscillation mainly originates from the cathode, as confirmed by the constant anode potential profile in Fig. S13 (SI), regardless of the presence of the spacer. Furthermore, under voltage oscillation, the mass flow from the outlet of the MEA followed the voltage oscillation and FE fluctuations, indicating that the pressure in the Cu GDE changes during operation (see Fig. S14, SI). The mass flow variation that can be induced by the gas chromatography measurements did not affect the oscillating behavior of the Cu GDE. The variations in pressure within the MEA can be attributed to the complete degradation of the Cu GDE. We further investigated the effects of electrolyte pH and temperature on the electrochemical performance of Cu GDE. In the case of the MEA operated at 0.1 M $KHCO_3$, a common trend across different current densities (100–200 mA cm^{-2}) was the increase in voltage, followed by a drastic voltage drop, accompanied by changes in CO_2R selectivity that corresponded to the voltage change. The magnitude of the voltage changes increased as repetitive voltage oscillation occurred. At a concentration of 1 M KOH (see Fig. S15, SI), the Cu GDE exhibited similar voltage oscillations, with a gradual increase in voltage change and a corresponding shift in selectivity. The main difference between the operation in 0.1 M $KHCO_3$ and 1 M KOH was the extent of operational time to reach the complete transition from CO_2R to HER. This observation is consistent with other studies reporting on the electrolyte concentration-dependent degradation behaviors of GDE. For example, Cofell *et al.* demonstrated that increasing the alkaline electrolyte concentration can result in increased salt precipitation and accelerating flooding.[20] El-Nagar *et al.* demonstrated that the K^+ concentration is a key parameter for K^+ crossing the membrane, influencing the selectivity of GDE with a current density dependency.[36] We also confirmed that elevating anolyte temperatures mitigates the complete transition from CO_2R to HER with decreased amplitude of voltage oscillation (see Fig. S16, SI).

Variations in predominant degradation mechanisms

The operation of the Cu GDE at a current density of −200 mA cm^{-2} revealed three distinct regions in the voltage–time profile (see Fig. 4a). Initially, a cathodic shift in potential was observed over the first 50 minutes, likely due to the precipitation, similar to the behavior observed at a current density of −150 mA cm^{-2}

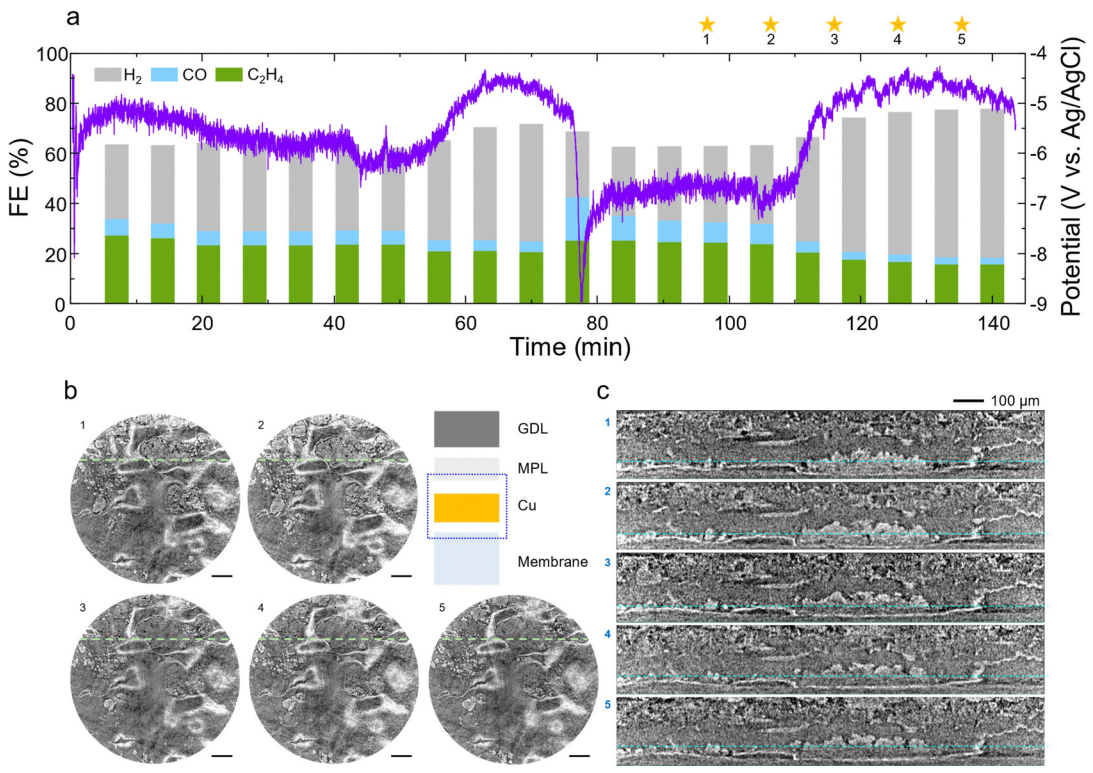

Fig. 4 Dissolution and regrowth of precipitates and flooding during eCO_2R. (a) FE and chronopotentiometry curve of Cu GDE at a current density of −200 mA cm^{-2} in 0.1 M $KHCO_3$. (b) 2D X-ray tomography images of MPL/Cu/membrane interface at points 1–5. The positions of the 2D images are indicated by the cyan dotted line in c. (c) Cross-sectional tomography images. The positions of the cross-sectional images are indicated by the green dotted line in b.

(see Fig. 3a). Following this, the potential shifted significantly to the anodic direction between 50 and 70 minutes, accompanied by an increase in H_2 selectivity. Between 75 and 80 minutes, a sharp potential drop occurred, along with fluctuations in FE:CO selectivity increased, H_2 selectivity decreased, and C_2H_4 selectivity remained relatively stable. This oscillatory behavior suggests that the salt precipitates formed within the Cu GDE dissolved, leading to restored catalytic activity for eCO_2R. Notably, the potential remained lower than the initial state, implying that the salt precipitates were not fully dissolved. Subsequently, the potential shifted anodically again between 100 and 120 minutes, along with a further increase in H_2 selectivity. The Cu GDE exhibited the FE distribution characterized by a decrease in CO_2R product selectivity and an increase in H_2 selectivity, indicating a shift from CO_2R to HER.

To further investigate the continuous increase in H_2 selectivity, we focused on the behavior of Cu GDE during the operation between 100 and 150 minutes. Fig. 4b presents selected 2D micro-CT images of the Cu GDE at the AEM/Cu/MPL interfaces. By comparing the images marked with dotted lines, it is evident that the shift to higher potential coincides with the dissolution of salt precipitates, which appeared with faint contrast. A series of cross-sectional micro-CT images further confirmed the dissolution of these salt precipitates from points 2 to 5 (Fig. 4c). Similar to the images shown in Fig. 3d, where Cu GDE exhibited oscillatory behavior, the flooding phenomenon was identified as the primary cause of the observed degradation, which in turn led to the transition from CO_2R to HER. As shown in Fig. S17 (SI), the Ag GDE exhibits similar oscillatory behavior with increasing H_2 selectivity, as voltage oscillation recurs, implying that the progression of degradation in MEA can be a universal phenomenon, regardless of the catalyst material.

Flooding as a predominant degradation mechanism

When the Cu GDE transitions from CO_2R to HER, a significant increase in H_2 selectivity, a decrease in CO_2R selectivity, and a shift in voltage toward anodic direction are observed. These electrochemical performances suggest that the predominant degradation mechanism at higher current densities differs from that at lower current densities. As shown in Fig. S18 (SI), the operation at -400 mA cm^{-2} in 0.1 M $KHCO_3$ showed dominant H_2 selectivity at the beginning and gradually transitioned from CO_2R to complete HER. Shi *et al.* compared the wettability of Au/C electrodes at different potentials and demonstrated a transition to a hydrophilic surface under more negative potentials.[32]

To investigate this further, we conducted X-ray tomography measurements of the MEA at a high operating current density of -250 mA cm^{-2} in 1 M $KHCO_3$. Initially, the potential shifted to a lower level during the first $\sim$15 minutes, then moved toward a higher (anodic) level during the subsequent 100 minutes of operation (see Fig. 5a). Corresponding with the voltage change, H_2 selectivity gradually increased over 100 minutes of operation, reaching 70%, while CO and C_2H_4 selectivity decreased (see Fig. 5b).

By comparing the cross-sectional micro-CT images acquired at points 1 and 2, we observed that the hollow spots in MPL, which appeared darker, showed contrast changes without significant precipitate formation at the Cu/membrane interface

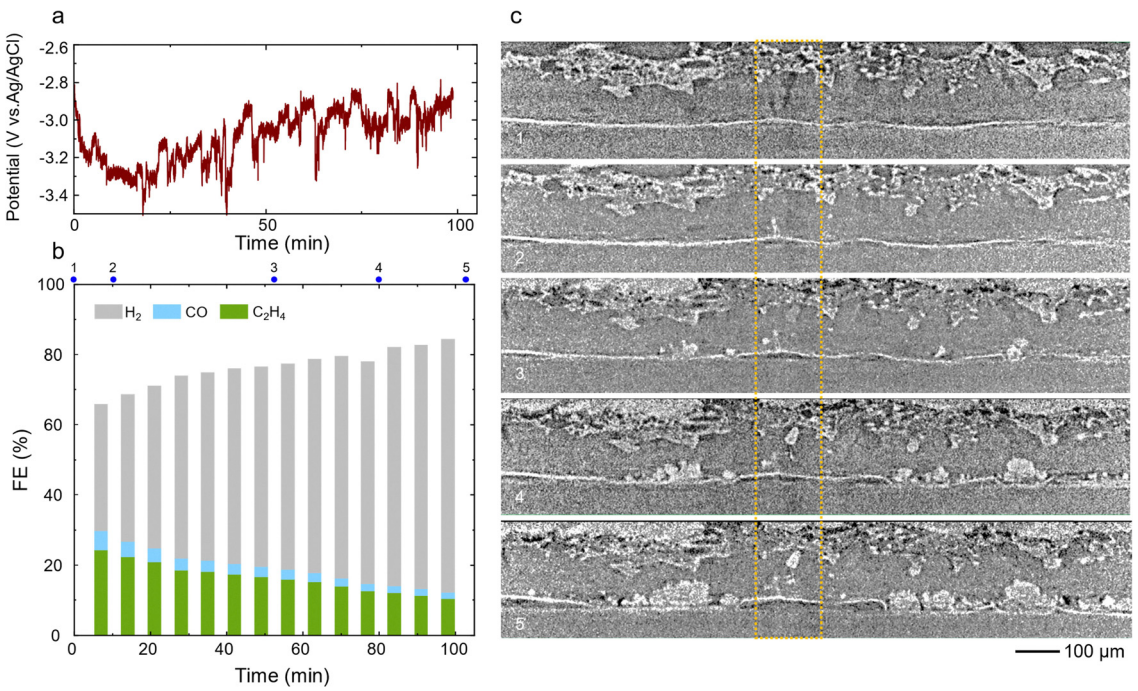

Fig. 5 Cu GDE operating at -250 mA cm^{-2} in 1 M $KHCO_3$. (a) Voltage–time profile. (b) Faradaic efficiency of CO_2R and HER. (c) Cross-sectional micro-CT images corresponding to the marked points in b. The yellow dotted line highlights the area of electrolyte flooding.

(see Fig. 5c). This suggests that water crossover (flooding) reached the MPL/GDL and promoting HER. While there is poor micro-CT contrast between pure water and GDE components in our cell, combining electrochemical data with X-ray tomography images provided valuable insights into the behavior under flooding conditions.

After 30 minutes of operation, the salt precipitates, seen as bright signals near the Cu/MPL region, were confirmed. Additionally, the interface between the Cu GDE and the membrane became rougher, revealing gaps. Compared to the hollow spots in MPL (point 1, marked with an orange dotted line), the same area showed a brighter signal, indicating that anolyte cations had reached the MPL/GDL. As the operating time increased, the growth of precipitates became more pronounced, as seen in images taken at points 3 to 5. Although the increase in precipitates may correlate with eCO_2R properties, the rapid transition from CO_2R to HER suggests that flooding, rather than precipitation, might be the primary degradation mechanism.

Multiphysics modeling of MEA during eCO_2R

A 1-D multiphysics model was built and solved using the commercial finite element method (FEM) software COMSOL to investigate the cause of precipitation, flooding and the resulting changes in selectivity. The model coupled dissolved species transport in the liquid phase, gas species transport and the electrochemical reaction kinetics at the cathode/anode. For details of the model setup, including geometry (Fig. S19, SI), governing equations, boundary conditions and parameters assignment, please refer to the section in SI: multiphysics modeling of MEA during eCO_2R.

Fig. 6a shows the ionic product value of the K_2CO_3 salt $Q_{K_2CO_3} = [K^+]^2[CO_3^{2-}]$ under different current densities. The solubility product K_{sp} = 2073 (M^3) of the K_2CO_3 is used as the criterion for precipitation.[16] In the case of −100 mA cm^{-2}, −150 mA cm^{-2} and −200 mA cm^{-2}, regions with $Q_{K_2CO_3} > K_{sp}$ near the AEM/CL interface can be seen, which indicates that thermodynamically, the K^+ and CO_3^{2-} ion concentration could facilitate the formation of precipitates in these regions. This is

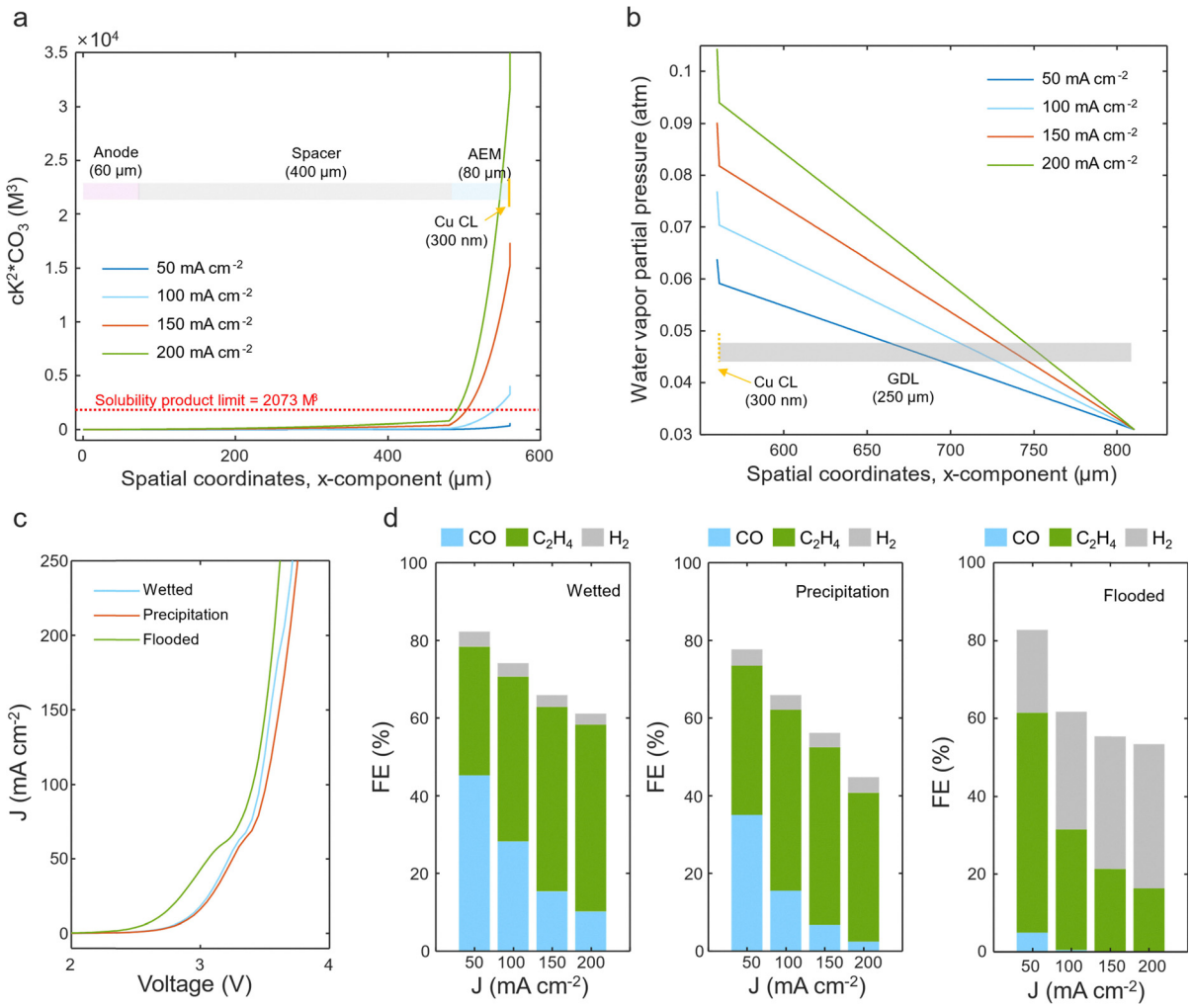

Fig. 6 Multiphysics simulation of the MEA failure mechanisms and their influence on CO_2R performance. (a) Simulated ionic product of the K_2CO_3. (b) Simulated water vapor partial pressure. (c) Simulated polarization curve demonstrating the influence of precipitation and flooding on voltage. (d) Simulated faradaic efficiency demonstrating the influence of precipitation and flooding on selectivity.

consistent with the experimental observation of the obvious fluctuation in voltage and selectivity and the precipitation under X-ray tomography images when operating -100 mA cm^{-2}, -150 mA cm^{-2} and -200 mA cm^{-2}. Fig. 6b shows the water vapor partial pressure distribution in the cathode diffusion medium. As the current density increases, the water vapor partial pressure also increases, which promotes the chance of flooding.

To investigate the influence of precipitation and flooding on voltage and selectivity of the cell, we carried out the simulation with three different assumptions: (1) the entire catalyst layer is wetted, having both liquid phase and gas phase with an active surface area density of 1×10^7 m^{-1}, representing the case with no precipitation or flooding; (2) the entire catalyst layer is wetted, but with a reduced active surface area density of 5×10^6 m^{-1}, representing the scenario where precipitates blocks part of the reaction sites; (3) only liquid phase transfer are assumed at the leftmost 250 μm of the catalyst layer and both liquid phase and gas phase transfer are assumed for the remaining 50 μm, representing the scenario where flooding occurs. Fig. 6c and d shows the simulated polarization curve and selectivity under these different assumptions. Comparing the simulation results of scenario (1) and (2), it could be seen that the blockage of surface area by precipitation could cause the voltage to shift to a more negative potential and a decrease in CO selectivity. Comparing scenario (1) and (3), it could be inferred that the flooding of the catalyst layer could cause a significant increase in H_2 selectivity and decrease in CO and C_2H_4 selectivity. This could be attributed to the decrease in CO_2 concentration in the catalyst layer due to the slow dissolved CO_2 diffusion rate in aqueous phase when flooded compared to the higher CO_2 concentration when gaseous pathways are available, which is proven by simulation when comparing the CO_2 concentration plotted in Fig. S20 and S21 (SI). Increasing electrolyte concentration can impact dissolved species profile and lead to increased precipitation within GDE, as shown in Fig. S22 (SI).

Conclusions

Operando X-ray tomography, combined with real-time electrochemical CO_2 reduction measurement, provided valuable insights into the predominant failure mechanisms during MEA operation. As shown in Fig. 7a, the eCO_2R process can be categorized into 3 cases: (1) increased HER with more negatively shifted cell potential (case A), (2) voltage oscillation

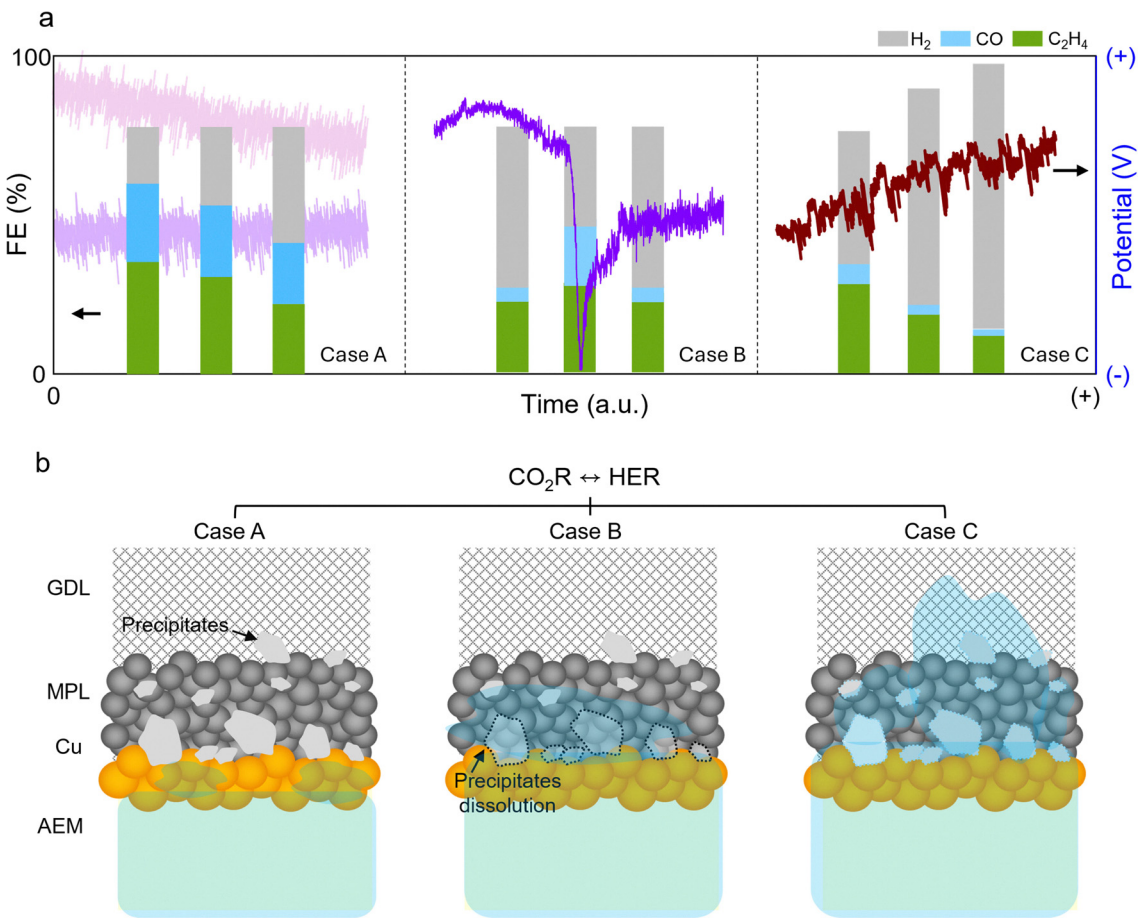

Fig. 7 Proposed relationship between eCO_2R properties and predominant degradation mechanisms. (a) Electrochemical voltage changes and the resulting CO_2R selectivity. (b) Schematic illustration of the degradation mechanism observed in each case.

and following transient selectivity change (case B), and (3) shift from CO_2R to H_2 production followed by anodically shifted cell potential (case C). Fig. 7b illustrates representative degradation phenomena for each case.

In case A, we observed inhomogeneous precipitate formation at the Cu/membrane interface. The extent of precipitate growth varied depending on the operating current density, with increased HER attributed to predominant precipitation. Low operating current density can result in a potential shift toward cathodic direction (pale pink line), and high operating current density (bright purple line) can maintain the potential while the eCO_2R product distribution decreases. In case B, where the MEA is near the stability threshold, partial dissolution of precipitates occurs near the Cu/membrane interfaces, coinciding with voltage oscillations. This leads to a transient change between CO_2R and HER. In case C, at high current densities or under high electrolyte concentrations, rapid water crossover reaches the GDL, promoting H_2 production rather than CO_2R. Flooding predominates over precipitation in this case, leading to an anodically shifted voltage. Understanding the failure mechanisms of the MEA reveals that these phenomena can be mitigated through the strategic engineering of components and optimization of operational conditions. In terms of component design, it is essential to develop GDEs with stable hydrophobicity and effective through-plane conductivity to prevent precipitation and flooding. Considering that the precipitation and flooding were mainly observed in the MPL, improving the hydrophobicity of MPL can contribute to enhanced CO_2R stability. GDEs with improved hydrophobicity should feature smooth surfaces since trenches in commercial GDEs can promote pH gradients and become sites for precipitation and flooding. The use of bipolar membranes that selectively permeate ions may also help alleviate these issues. Operational optimization may involve investigating the effects of cations in the anolytes, as cation crossover through the membrane depends on the size of the cations. Additionally, acidic electrolytes can suppress salt precipitation, although this requires the development of CO_2R-selective catalysts to minimize HER interference.

In summary, we investigated the degradation behavior of the MEA, focusing on precipitation and flooding using *operando* X-ray tomography coupled with real-time electrochemical measurement. X-ray tomography enabled us to visualize interface dynamics at solid/liquid/gas boundaries and track the phase distribution within the MEA, significantly enhancing our understanding of degradation mechanisms through structural changes over time. We categorized the predominant degradation behaviors into three cases by correlating voltage profiles, selectivity distributions, and morphological changes in the MEA caused by water crossover and precipitation. Key findings include: (1) visualization of growth and dissolution of precipitates in Cu GDE, providing deeper insights into the mechanisms of MEA failure. (2) Tracking mechanical deformation at the Cu GDE/membrane interface due to precipitation and flooding, which has not been previously observed. (3) Providing direct visual evidence of the transition from CO_2R to HER, with a focus on the distribution of precipitates and water crossover from the catalyst/membrane interface to the GDL.

Understanding and mitigating precipitate formation and flooding mechanisms is critical for scaling eCO_2R technology for industrial applications. Persistent flooding and salt formation not only reduce system efficiency and catalyst lifetime but also increase operational costs and maintenance requirements. By identifying key failure pathways, our study provides insights that can guide the design of more durable MEAs, ultimately improving the viability of eCO_2R for large-scale carbon utilization.

Experimental

Preparation of electrode

Carbon paper with a PTFE microporous layer (Sigracet 28BC), purchased from the Fuel Cell Store, was used as gas diffusion electrode. Cu catalysts were deposited onto the GDE using a dielectric sputtering system (ATC Orion 8, AJA International). The deposition process was carried out at a pressure of 5 mTorr, with a power of 100 W. Argon (Ar) gas was used at a flow rate of 20 standard cubic centimeters per minute (sccm), and the Cu deposition was performed for 90 minutes.

Characterization

The morphology of the Cu GDE was examined using FEI Nova NanoSEM 450, operating with a 10 kV electron beam. The crystal structure of the Cu GDE was investigated through X-ray diffraction (XRD) using Bruker DISCOVER D8 diffractometer equipped with Cu Kα radiation. Diffraction data were collected using a two-dimensional dimensional VÅNTEC-500 detector and subsequently integrated into one-dimensional patterns using DIFFRAC.SUITE™ EVA software.

Electrochemical carbon dioxide reduction measurement

Electrochemical carbon dioxide reduction measurement was performed using a mass flow controller (Alicat), a gas humidifier, a custom-designed reactor made of PEEK, a peristaltic pump, and a mass flow meter (Alicat). The outlet of the mass flow meter was connected to a gas chromatograph for analyzing gaseous products. The reactor consists of a cylindrical anode and cathode chamber without a flow channel, a Pt-coated Ti mesh as anode, a Cu GDE cathode, and a grid-patterned Nylon spacer. The spacer was placed between the anode and PiperION 60 anion exchange membrane (AEM) to minimize metal signal interference during X-ray tomography measurements. The titanium rods served as the current collector for both anode and cathode. The anodic chamber was supplied with 0.1 M $KHCO_3$ at a constant flow rate of 30 ml min^{-1}. The cathode chamber was fed with humidified CO_2 at a flow rate of 30 sccm. The cell had an active area of 0.5 cm^2. Electrochemical CO_2R was carried out using a potentiostat (VSP200, Biologic) in a three-electrode setup: Cu GDE as the working electrode, Pt/Ti mesh as the counter electrode, and a leakless Ag/AgCl reference electrode.

Electrochemical impedance spectroscopy was conducted using a potentiostat (VSP 300, Biologic) at an applied potential of −2 V *vs.* Ag/AgCl with the amplitude of 10 mV, sweeping from 100 kHz to 1 Hz. The silicon (Si) and ethylene tetrafluoroethylene (ETFE) gaskets were used to seal the MEA, which was assembled using a torque wrench at 6 N m. All the bolts and nuts were made of plastic materials to prevent interference with the tomography imaging. The gaseous products were analyzed using gas chromatography (SRI-8610C) with Molsieve 5A and Hayesep D column. A flame ionization detector (FID), equipped with a methanizer, and a thermal conductivity detector (TCD) were used for detection.

X-ray tomography measurement

X-ray tomography measurement was performed using synchrotron instrumentation at Advanced Light Source (ALS) Beamline 8.3.2., Lawrence Berkeley National Laboratory (LBNL). The X-ray energy used was 38 keV, and the X-ray beam passed through the MEA and was subsequently converted into visible light by a scintillator. After image alignment, the region of interest (ROI) was defined, and the measurement were initiated. The image resolution (pixel size) was 0.65 μm and the exposure time was 200 ms. The MEA images were projected during a 180° rotation. Data reconstruction was performed at the National Energy Research Scientific Computing Center (NERSC). Following reconstruction, the images were processed and visualized using Fiji and Dragonfly Software.

Computational details

In order to provide theoretical support to the experimental observation of precipitation and flooding phenomenon and their impact on voltage and selectivity, a 1-D multiphysics model was built and solved using the commercial finite element method (FEM) software COMSOL Multiphysics (version 6.2). The model is an adaptation of the models developed for CO_2R electrolyzers by Weng *et al.*[37–39] and is consisted of the ion and gas species transport, the electrochemical reaction kinetics and phase transport between gas and liquid phase.

Geometry. The geometry of the model is demonstrated in Fig. S19 (SI), including (from left to right) a porous electrode domain as the anode (60 μm), a spacer domain (50 μm), an AEM domain (80 μm), a Cu catalyst layer (CL) domain (300 nm in total) consisted of a flooded section and a wetted section, and a cathode diffusion medium (cDM) domain (250 μm). The length of the flooded section and the wetted section is adjusted according to the status we want to investigate, but the two sections add up to be 300 nm in length. In a non-flooded case, the flooded section length is set to be a very low value of 2 nm and the rest 298 nm is wetted. In a flooded case, the flooded section length is set to be 250 nm and the rest 50 nm is wetted. The meshing of the model consists of a total of 5600 elements with a minimum size of 0.01 nm. The closer it is to the interface between different domains, the finer the meshes are, while relatively coarser meshes are applied at the middle of the domains.

Governing equations. The domains can be categorized into aqueous phase domains (including anode, spacer, AEM and flooded CL domains), gas phase domain (cDM domain) and mixed phase domain (wetted CL domain). The aqueous phase domains features the transport of dissolved CO_2 and ion species (K^+, H^+, OH^-, HCO_3^-, CO_3^{2-}) governed by Nernst–Planck equation, which can be expressed as the dependence of the molar flux, N_i, on the concentration c_i of species i and the electrolyte potential ϕ_l,

$$\boldsymbol{N}_i = -D_i^{\text{eff}}\nabla c_i - \frac{z_i F}{RT} D_i^{\text{eff}} c_i \nabla \phi_l \tag{1}$$

where D_i^{eff} is the effective diffusion coefficient in porous medium, z_i is the charge number of species i, F is the Faraday constant (9.648×10^4 C mol^{-1}), R is the ideal gas constant and T is the room temperature (293.15 K). And the flux satisfies

$$\nabla \cdot \boldsymbol{N}_i = R_i \tag{2}$$

where R_i is the reaction rate which could include bulk phase reactions, electrode reactions and phase transfer reactions, which will be discussed in the later paragraphs.

The gas phase domains feature the mixture-averaged transport model for the gas species (CO_2, H_2, CO, C_2H_4),

$$\boldsymbol{N}_j = \frac{1}{M_j}\left(-\rho_G D_j^{\text{eff}}\nabla\omega_j - \rho_G D_j^{\text{eff}}\omega_j\frac{\nabla M_A}{M_A}\right) \tag{3}$$

where ρ_G is the gaseous mixture density; M_j, ω_j, D_j^{eff} is the molar mass, mass fraction and effective diffusion coefficient respectively; $M_A = \left(\sum_j \frac{\omega_j}{M_j}\right)^{-1}$ is the average molecular weight of the mixture. Note that even though CH_4 could be present in our system, it is excluded for simplicity from our simulation together with its evolution reaction since we barely observe it in our experiment.

In the bulk aqueous phase, the dissolved inorganic carbon (DIC) species are dynamically converting to each other according to the reactions and the reaction rate constants from the paper by Schulz and Zeebe *et al.*[40]

The following cathodic reactions are considered at Cu catalyst layer:

$$2H_2O + 2e^- \rightarrow H_2 + 2OH^- \tag{4}$$

$$CO_2 + H_2O + 2e^- \rightarrow CO + 2OH^- \tag{5}$$

$$2CO_2 + 8H_2O + 12e^- \rightarrow C_2H_4 + 12OH^- \tag{6}$$

$$2CO_2 + 9H_2O + 12e^- \rightarrow C_2H_5OH + 12OH^- \tag{7}$$

The oxygen evolution reaction (OER) is assumed to happen at the anode:

$$2H_2O \rightarrow O_2 + 4H^+ + 4e^- \tag{8}$$

The partial current densities of the above charge transfer reactions follow the Tafel kinetics,

$$i_k = i_{0,k}\prod_i\left(\frac{c_i}{1[\text{M}]}\right)^{\gamma_{i,k}}\exp\left(-\frac{\alpha_k F}{RT}\eta_k\right) \tag{9}$$

where η_k is the overpotential, defined as $\eta_k = \phi_s - \phi_l - E_{eq}$. The electric potential, ϕ_s, and the electrolyte potential, ϕ_l, are variables determined by eqn (1). The reaction kinetics parameters, exchange current density $i_{0,k}$, concentration dependence $\left(\frac{c_i}{1[M]}\right)^{\gamma_{i,k}}$ and charge transfer coefficient α_k are used as the same values as the ref. 39.

The mixed phase domain has both Nernst–Planck equation and the mixture average equation, along with the phase transport of dissolved CO_2, governed by

$$R^{PT}_{CO_2} = a_s k_{CO_2}\left(c_{CO_2,l} - H_{CO_2} p_{CO_2}\right) \quad (10)$$

a_s is the surface area density (1×10^7 m^{-1}), k_{CO_2} is the phase transfer coefficient of CO_2 (0.1 cm s^{-1}) and H_{CO_2} is the Henry's constant (0.034 M atm^{-1}). $c_{CO_2,l}$ is the aqueous CO_2 concentration, and p_{CO_2} is the partial pressure of CO_2 calculated from ω_j.

Author contributions

S. A. L. wrote the manuscript with the assistance of W. D., H. A. A., and C. X. I. S. and M. J. J. contributed to the design of the electrochemical cell for X-ray tomography imaging. S. A. L., M. J. J., and Z. Q. performed the electrochemical CO_2 reduction and X-ray tomography measurements with the assistance of L. P.-F. and D. Y. P. K. W. contributed to the simulation of the electrochemical cell. W. D. and C. X. conceived the project. W. D., H. A. A. and C. X. supervised the project. All authors discussed the results and commented on the manuscript.

Conflicts of interest

The authors declare no conflicts of interest.

Data availability

The data supporting this article have been inlcuded as part of the SI.

Supplementary information is available. See DOI: **https://doi.org/10.1039/d5ey00232j**

Acknowledgements

This work was performed by the Liquid Sunlight Alliance, which is supported by the U.S. Department of Energy, Office of Science, Office of Basic Energy Sciences, Fuels from Sunlight Hub, under Grant DE-SC0021266. This research used resources of the Advanced Light Source, which is a DOE Office of Science User Facility under contract no. DE-AC02-05CH11231.

References

1 S. Garg, M. Li, A. Z. Weber, L. Ge, L. Li, V. Rudolph, G. Wang and T. E. Rufford, *J. Mater. Chem. A*, 2020, **8**, 1511–1544.
2 L. Ge, H. Rabiee, M. Li, S. Subramanian, Y. Zheng, J. H. Lee, T. Burdyny and H. Wang, *Chem*, 2022, **8**, 663–692.
3 T. Burdyny and W. A. Smith, *Energy Environ. Sci.*, 2019, **12**, 1442–1453.
4 M. E. Leonard, L. E. Clarke, A. Forner-Cuenca, S. M. Brown and F. R. Brushett, *ChemSusChem*, 2020, **13**, 400–411.
5 H. Rabiee, L. Ge, X. Zhang, S. Hu, M. Li and Z. Yuan, *Energy Environ. Sci.*, 2021, **14**, 1959–2008.
6 S. Nitopi, E. Bertheussen, S. B. Scott, X. Liu, A. K. Engstfeld, S. Horch, B. Seger, I. E. L. Stephens, K. Chan, C. Hahn, J. K. Nørskov, T. F. Jaramillo and I. Chorkendorff, *Chem. Rev.*, 2019, **119**, 7610–7672.
7 J.-J. Lv, M. Jouny, W. Luc, W. Zhu, J.-J. Zhu and F. Jiao, *Adv. Mater.*, 2018, **30**, 1803111.
8 D. A. Henckel, M. J. Counihan, H. E. Holmes, X. Chen, U. O. Nwabara, S. Verma, J. Rodríguez-López, P. J. A. Kenis and A. A. Gewirth, *ACS Catal.*, 2021, **11**, 255–263.
9 J. A. Abarca, G. Díaz-Sainz and A. Irabien, *J. CO2. Util.*, 2024, **86**, 102897.
10 M. Li, M. N. Idros, Y. Wu, T. Burdyny, S. Garg, X. S. Zhao, G. Wang and T. E. Rufford, *J. Mater. Chem. A*, 2021, **9**, 19369–19409.
11 B. De Mot, M. Ramdin, J. Hereijgers, T. J. H. Vlugt and T. Breugelmans, *ChemElectroChem*, 2020, **7**, 3839–3843.
12 B. Endrődi, E. Kecsenovity, A. Samu, F. Darvas, R. V. Jones, V. Török, A. Danyi and C. Janáky, *ACS Energy Lett.*, 2019, **4**, 1770–1777.
13 D. G. Wheeler, B. A. W. Mowbray, A. Reyes, F. Habibzadeh, J. He and C. P. Berlinguette, *Energy Environ. Sci.*, 2020, **13**, 5126–5134.
14 M. Sassenburg, M. Kelly, S. Subramanian, W. A. Smith and T. Burdyny, *ACS Energy Lett.*, 2023, **8**, 321–331.
15 R. Casebolt, K. Levine, J. Suntivich and T. Hanrath, *Joule*, 2021, **5**, 1987–2026.
16 Y. Xu, J. P. Edwards, S. Liu, R. K. Miao, J. E. Huang, C. M. Gabardo, C. P. O'Brien, J. Li, E. H. Sargent and D. Sinton, *ACS Energy Lett.*, 2021, **6**, 809–815.
17 Q. Xu, A. Xu, S. Garg, A. B. Moss, I. Chorkendorff, T. Bligaard and B. Seger, *Angew. Chem., Int. Ed.*, 2023, **62**, e202214383.
18 A. B. Moss, J. Hätinen, P. Kúš, S. Garg, M. Mirolo, I. Chorkendorff, B. Seger and J. Drnec, *J. Power Sources*, 2023, **562**, 232754.
19 K. Krause, J. K. Lee, C. Lee, H. W. Shafaque, P. J. Kim, K. F. Fahy, P. Shrestha, J. M. LaManna, E. Baltic, D. L. Jacobson, D. S. Hussey and A. Bazylak, *J. Power Sources*, 2022, **520**, 230879.
20 E. R. Cofell, U. O. Nwabara, S. S. Bhargava, D. E. Henckel and P. J. A. Kenis, *ACS Appl. Mater. Interfaces*, 2021, **13**, 15132–15142.
21 L. Bohn, J. Häberlein, F. Brendel, L. Metzler, L. Helfen, A. Tengattini, C. Klose, S. Vierrath and J. Disch, *ACS Energy Lett.*, 2025, **10**, 975–981.
22 B. Endrődi, A. Samu, E. Kecsenovity, T. Halmágyi, D. Sebők and C. Janáky, *Nat. Energy*, 2021, **6**, 439–448.
23 S. Hao, A. Elgazzar, N. Ravi, T.-U. Wi, P. Zhu, Y. Feng, Y. Xia, F.-Y. Chen, X. Shan and H. Wang, *Nat. Energy*, 2025, **10**, 266–277.

24 A. B. Moss, S. Garg, M. Mirolo, C. A. Giron Rodriguez, R. Ilvonen, I. Chorkendorff, J. Drnec and B. Seger, *Joule*, 2023, **7**, 350–365.
25 J. Disch, L. Bohn, S. Koch, M. Schulz, Y. Han, A. Tengattini, L. Helfen, M. Breitwieser and S. Vierrath, *Nat. Commun.*, 2022, **13**, 6099.
26 J. T. Lang, D. Kulkarni, C. W. Foster, Y. Huang, M. A. Sepe, S. Shimpalee, D. Y. Parkinson and I. V. Zenyuk, *Chem. Rev.*, 2023, **123**, 9880–9914.
27 C. P. O'Brien, D. McLaughlin, T. Böhm, Y. C. Xiao, J. P. Edwards, C. M. Gabardo, M. Bierling, J. Wicks, A. Sedighian Rasouli, J. Abed, D. Young, C.-T. Dinh, E. H. Sargent, S. Thiele and D. Sinton, *Joule*, 2024, **8**, 2903–2919.
28 V. Wood, *Nat. Rev. Mater.*, 2018, **3**, 293–295.
29 Y. Wu, L. Charlesworth, I. Maglaya, M. N. Idros, M. Li, T. Burdyny, G. Wang and T. E. Rufford, *ACS Energy Lett.*, 2022, **7**, 2884–2892.
30 J. Disch, L. Bohn, L. Metzler and S. Vierrath, *J. Mater. Chem. A*, 2023, **11**, 7344–7357.
31 L. Hoof, N. Thissen, K. Pellumbi, K. Junge Puring, D. Siegmund, A. K. Mechler and U.-P. Apfel, *Cell Rep. Phys. Sci.*, 2022, **3**, 100825.
32 R. Shi, J. Guo, X. Zhang, G. I. N. Waterhouse, Z. Han, Y. Zhao, L. Shang, C. Zhou, L. Jiang and T. Zhang, *Nat. Commun.*, 2020, **11**, 3028.
33 L. M. Baumgartner, C. I. Koopman, A. Forner-Cuenca and D. A. Vermaas, *ACS Appl. Energy Mater.*, 2022, **5**, 15125–15135.
34 Y. Wu, H. Rabiee, X. S. Zhao, G. Wang and Y. Jiang, *J. Mater. Chem. A*, 2024, **12**, 14206–14228.
35 N. Mikami, K. Morishita, T. Murakami, T. Hosobata, Y. Yamagata, T. Ogawa, Y. Mukouyama, S. Nakanishi, J. W. I. Ager, K. Fujii and S. Wada, *ACS Energy Lett.*, 2024, **9**, 4225–4232.
36 G. A. El-Nagar, F. Haun, S. Gupta, S. Stojkovikj and M. T. Mayer, *Nat. Commun.*, 2023, **14**, 2062.
37 L.-C. Weng, A. T. Bell and A. Z. Weber, *Energy Environ. Sci.*, 2019, **12**, 1950–1968.
38 L.-C. Weng, A. T. Bell and A. Z. Weber, *Phys. Chem. Chem. Phys.*, 2018, **20**, 16973–16984.
39 L.-C. Weng, A. T. Bell and A. Z. Weber, *Energy Environ. Sci.*, 2020, **13**, 3592–3606.
40 K. G. Schulz, U. Riebesell, B. Rost, S. Thoms and R. E. Zeebe, *Mar. Chem.*, 2006, **100**, 53–65.